

Oxygen activation-triggered thermal instability in $Li(Ni_{0.8}Co_{0.1}Mn_{0.1})O_2$ cathode

Supeng Chen(陈苏鹏), Yingli Li(李英丽), Yande Li(李彦德), Keqiang Li(李克强), Peirong Li(李培荣), Jianwei Meng(孟建伟), Zilong Zhao(赵子龙), Yuanyuan Pan(潘圆圆), Qinghao Li(李庆浩), and Pengfei Yu(于鹏飞)
Citation: Chin. Phys. B, 2025, 34 (**10**): 108201. DOI: 10.1088/1674-1056/ae0436
http://cpb.iphy.ac.cn; http://iopscience.iop.org/cpb

What follows is a list of articles you may be interested in

Al-Zr dual-doping enhancing the electrochemical performance of spinel $LiMn_2O_4$ cathodes

Wei Wu(吴伟), Yuhui Cui(崔煜辉), Yuxin Zheng(郑雨欣), Fei Huang(黄飞), Hong Li(李泓), and Liang Yin(尹良)
Chin. Phys. B, 2025, 34 (**6**): 068201. DOI: 10.1088/1674-1056/adc085

Synergistic bulk and surface engineering via rapid quenching for high-performance Li-rich layered manganese oxide cathodes

Xinyun Xiong(熊馨筠), Sichen Jiao(焦思晨), Qinghua Zhang(张庆华), Luyao Wang(王璐瑶), Kun Zhou(周坤), Bowei Cao(曹博维), Xilin Xu(徐熙林), Xiqian Yu(禹习谦), and Hong Li(李泓)
Chin. Phys. B, 2025, 34 (**5**): 058201. DOI: 10.1088/1674-1056/adc673

Significant increase in thermal conductivity of cathode material $LiFePO_4$ by Na substitution: A machine learning interatomic potential-assisted investigation

Shi-Yi Li(李诗怡), Qian Liu(刘骞), Yu-Jia Zeng(曾育佳), Guofeng Xie(谢国锋), and Wu-Xing Zhou(周五星)
Chin. Phys. B, 2025, 34 (**2**): 028201. DOI: 10.1088/1674-1056/ad9e99

Defect chemistry engineering of Ga-doped garnet electrolyte with high stability for solid-state lithium metal batteries

Sihan Chen(陈思汗), Jun Li(黎俊), Keke Liu(刘可可), Xiaochen Sun(孙笑晨), Jingwei Wan(万京伟), Huiyu Zhai(翟慧宇), Xinfeng Tang(唐新峰), and Gangjian Tan(谭刚健)
Chin. Phys. B, 2024, 33 (**8**): 088203. DOI: 10.1088/1674-1056/ad41b9

Surface encapsulation of layered oxide cathode material with $NiTiO_3$ for enhanced cycling stability of Na-ion batteries

Zilin Hu(胡紫霖), Bin Tang(唐彬), Ting Lin(林挺), Chu Zhang(张楚), Yaoshen Niu(牛耀申), Yuan Liu(刘渊), Like Gao(高立克), Fei Xie(谢飞), Xiaohui Rong(容晓晖), Yaxiang Lu(陆雅翔), and Yongsheng Hu(胡勇胜)
Chin. Phys. B, 2024, 33 (**8**): 088202. DOI: 10.1088/1674-1056/ad50c2

RAPID COMMUNICATION

Oxygen activation-triggered thermal instability in $Li(Ni_{0.8}Co_{0.1}Mn_{0.1})O_2$ cathode

Supeng Chen(陈苏鹏)[1,†], Yingli Li(李英丽)[1,†], Yande Li(李彦德)[2,†], Keqiang Li(李克强)[1], Peirong Li(李培荣)[1], Jianwei Meng(孟建伟)[3], Zilong Zhao(赵子龙)[4,‡], Yuanyuan Pan(潘圆圆)[1,§], Qinghao Li(李庆浩)[1,¶], and Pengfei Yu(于鹏飞)[3,♯]

[1] *College of Physics, Qingdao University, Qingdao* 266071, *China*
[2] *National Synchrotron Radiation Laboratory, University of Science and Technology of China, Hefei* 230029, *China*
[3] *Center for Transformative Science, ShanghaiTech University, Shanghai* 201210, *China*
[4] *Shanghai Advanced Research Institute, Chinese Academy of Sciences, Shanghai* 201210, *China*

(Received 3 August 2025; revised manuscript received 28 August 2025; accepted manuscript online 8 September 2025)

Ni-rich layered $LiNi_{0.8}Co_{0.1}Mn_{0.1}O_2$ (NCM811) is a leading cathode candidate for the next generation of lithium-ion batteries because of its high energy density. In practice, NCM811 exhibits poor thermal stability that can lead to thermal runaway, which is a critical bottleneck for the practical application of this promising material. The fundamental factors underlying thermal failure and the relationship between surface and bulk degradation, however, remain unclear. In this work, we track the evolution of the atomic and electronic structures of high-voltage delithiated NCM811 using x-ray diffraction (XRD), transmission electron microscopy (TEM), and synchrotron-based soft x-ray absorption spectroscopy (sXAS). Oxygen hole states formed upon delithiation are thermodynamically unstable and lead to O_2 release upon heating. This O_2 release occurs prior to phase transitions and therefore constitutes the primary cause of thermal failure in NCM811 cathodes. Although surface oxygen is inherently less stable, the presence of similar oxygen hole states at the surface and in the bulk causes surface and bulk degradation to proceed almost simultaneously. These findings delineate the degradation pathway of NCM811 during thermal runaway and provide rational guidelines for material design and optimization.

Keywords: Ni-rich cathode, thermal decay, oxygen hole, soft x-ray spectroscopy

PACS: 82.47.Aa, 82.45.Fk, 78.70.Dm, 68.60.Dv

DOI: 10.1088/1674-1056/ae0436 **CSTR:** 32038.14.CPB.ae0436

1. Introduction

With the rapid advancement of renewable energy technologies, lithium-ion batteries (LIBs) have become the dominant energy storage technology. Their applications have expanded from portable electronics and electric vehicles (EVs) to grid-scale energy storage, with energy storage density increasing rapidly over the past decades. At present, Ni-rich layered $LiNi_{0.8}Co_{0.1}Mn_{0.1}O_2$ (NCM811) is widely regarded as one of the most promising cathode candidates for the next generation of LIBs, capable of supporting long-distance EVs.[1] Ni-rich cathodes exhibit large specific capacities (200–250 mAh/g) and high operating voltages ($\sim$ 4.3 V vs. Li^+/Li), but they suffer from unsatisfactory thermal stability at high states of charge. Thermal runaway involves a series of complex exothermic reactions under overcharging, short-circuiting, or high-temperature conditions, which can potentially lead to fires or even explosions. The thermal instability of NCM811 and the associated safety concerns present a critical bottleneck for its practical development.[2]

Improving the thermal stability of Ni-rich layered cathodes critically depends on a comprehensive understanding of the origins of their thermal instability. The most direct cause of thermal instability is oxygen release from highly delithiated cathodes upon heating, which subsequently reacts with electrolytes and anodes.[3] The oxygen release is strongly correlated with the transition-metal (TM) composition, and the amount of evolved oxygen increases with higher Ni content.[4,5] However, the microscopic mechanism of oxygen release remains controversial. Some studies suggest that delithiated Ni-rich layered cathodes undergo a specific phase transformation pathway upon heating: from a layered (R-3m, L) to a spinel (Fd-3m, S), and finally to a rock-salt (Fm-3m, RS) structure, with oxygen released to maintain stoichiometry during such phase transitions.[1,4,6,7] Other studies argue that changes in the oxidation states and the resulting site preferences of TM cations are the key factors governing ther-

[†]These authors contributed equally to this work.
[‡]Corresponding author. E-mail: zhaozl@sari.ac.cn
[§]Corresponding author. E-mail: panyuanupc@126.com
[¶]Corresponding author. E-mail: qhli@qdu.edu.cn
[♯]Corresponding author. E-mail: yupf1@shanghaitech.edu.cn

© 2025 Chinese Physical Society and IOP Publishing Ltd. All rights, including for text and data mining, AI training, and similar technologies, are reserved.

mal stability. Thermodynamically unstable Ni^{4+} in delithiated Ni-rich cathodes tends to reduce to Ni^{2+} upon heating. This reduction is often accompanied by the migration of Ni^{2+} ions from the TM layer into the Li layer, which further triggers structural phase transitions and oxygen release.[5] Liu *et al.*[8] further reported that Co^{4+} ions tend to reduce prior to Ni^{4+} and can temporarily occupy tetrahedral sites, thereby delaying Ni migration and postponing oxygen release. Recent work has also emphasized that the generation of oxygen vacancies may be the fundamental origin of thermal instability. Oxygen loss occurs preferentially at the surface because of its intrinsic instability, leading to the formation of oxygen vacancies. These vacancies can subsequently propagate into the bulk, eventually triggering bulk oxygen loss and thermal failure.[9–11] Based on the above studies, it can be inferred that TM migration, structural reconstruction, and oxygen vacancy formation are usually intertwined, complicating the identification of the dominant factors for thermal stability. Moreover, the initiation and propagation of thermal instability from the surface to the bulk remain ambiguous. By combining transmission electron microscopy (TEM) and electron energy loss spectroscopy (EELS), Wei *et al.*[10] found that the concentration of oxygen vacancies, which corresponds to oxygen loss, between the surface and the bulk is negligible because of their high diffusion rate in Ni-rich systems. In contrast, Li *et al.*[11] observed a substantial delay in the thermal decomposition of the bulk compared with the particle surface through *in-situ* Raman and x-ray diffraction (XRD) measurements.

These discrepancies highlight the need for further investigation into the mechanisms governing the thermal degradation of Ni-rich layered cathodes. Soft x-ray absorption spectroscopy (sXAS) has proven to be a powerful tool in this field.[12,13] Soft XAS directly probes the unoccupied states near the Fermi level with well-resolved spectral features, making it highly sensitive to the valence states of 3d transition metals and the activated forms of oxygen.[14] The method can also provide spatially averaged information over relatively large sample areas, requires minimal sample preparation, and causes negligible beam damage, thus enabling clearer correlation of microscopic features with macroscopic material properties. Moreover, surface and bulk information can be simultaneously obtained by employing both total electron yield (EY) and fluorescence yield (FY) detection modes, which facilitates a more comprehensive understanding of their respective roles in thermal instability.[15–17] Such features make soft x-ray spectroscopy the tool of choice to investigate the detailed thermal decay behavior of NCM materials.

In this work, the thermal decay behavior of Ni-rich layered NCM811 is investigated by combining XRD, TEM, and synchrotron-based sXAS. The overall and local structural evolution of delithiated NCM811 is characterized from room temperature to 450 °C by XRD and TEM, respectively. Synchrotron-based sXAS was further employed to fingerprint element-state evolution from both surface and bulk perspectives throughout the thermal runaway process. By combining the element-specific variations observed in the O *K*-edge and Ni *L*-edge spectra with the structural evolution data obtained from XRD and TEM, we aim to identify the fundamental driving forces of thermal instability. In addition, simultaneous acquisition of surface and bulk information enables a rigorous comparison, allowing a more accurate correlation between surface and bulk behavior. The derived understanding provides critical insights into the thermal runaway behavior of Ni-rich layered cathodes and offers rational guidelines for material design and optimization.

2. Experiments

2.1. Materials synthesis

The precursor $Ni_{0.8}Co_{0.1}Mn_{0.1}(OH)_2$ for NCM811 was synthesized by a co-precipitation method. $NiSO_4{\cdot}6H_2O$, $CoSO_4{\cdot}7H_2O$, and $MnSO_4{\cdot}H_2O$ were dissolved in deionized water at a molar ratio of 8:1:1 to prepare a 2 M solution. This solution was slowly pumped into a 3 L flask under a N_2 atmosphere. Simultaneously, NaOH and $NH_3{\cdot}H_2O$ were slowly added to the flask to maintain a pH of 11.0. The reaction was carried out at 60 °C with continuous stirring at 300 rpm for 24 h. The resulting precipitate was filtered and dried to obtain the precursor $Ni_{0.8}Co_{0.1}Mn_{0.1}(OH)_2$. The precursor was then mixed and ground with $LiOH{\cdot}H_2O$ at a molar ratio of 1:1.05. The mixture was transferred to an alumina crucible and calcined in an O_2 atmosphere: first at 450 °C for 5 h, then at 730 °C for 10 h, with a heating rate of 5 °C/min. The resulting black powder was $LiNi_{0.8}Co_{0.1}Mn_{0.1}O_2$.

2.2. Delithiated materials preparation

NCM811 was prepared via electrochemical delithiation. The working electrode was composed of active material, PVDF binder, and conductive carbon in a mass ratio of 8:1:1. The electrode was assembled into CR2032 coin cells in an argon glovebox with O_2 and H_2O partial pressures below 1 ppm. The electrolyte was 1 M $LiPF_6$ in EC, DMC, and DEC with a volume ratio of 1:1:1. The coin cells were charged to 4.5 V, delivering a typical specific capacity of $\sim$ 190 mAh/g at room temperature, and were immediately disassembled in the glovebox to obtain $Li_{0.3}Ni_{0.8}Co_{0.1}Mn_{0.1}O_2$, denoted as $Li_{0.3}$NCM-25 °C. Delithiated NCM cathode samples were subsequently heated to 150 °C, 300 °C, and 450 °C for 10 min in an argon atmosphere, and were denoted as $Li_{0.3}$NCM-150 °C, $Li_{0.3}$NCM-300 °C, and $Li_{0.3}$NCM-450 °C, respectively.

2.3. Structural and valence state characterization

The crystal structures of the samples were characterized by XRD (Rigaku Bruker D8 Advance) with Cu $K\alpha$ (λ = 1.5406 Å) radiation from $2\theta = 10^\circ$ to 70° at a scanning rate

of 2 °/min. The morphology and microstructure of the particles were characterized by SEM (JEOL JSM-6700F) and TEM (JEOL JEM-2100F). The coordination environment and valence states of the elements were analyzed by synchrotron-based sXAS and x-ray photoelectron spectroscopy (XPS) (PHI 5000 Versaprobe III). The sXAS data were collected at beamline BL02B of the Shanghai Synchrotron Radiation Facility (SSRF). The samples were transferred through an argon-filled chamber to avoid exposure to air. The measurements were performed at room temperature in total electron yield (TEY) and partial fluorescence yield (PFY) modes simultaneously.

3. Results and discussion

To characterize the overall crystallinity, Fig. 1(a) shows the XRD pattern of pristine NCM811 with diffraction peaks at 18.67°, 36.58° and 44.36°, corresponding to the $(003)_R$, $(101)_R$ and $(104)_R$ peaks within the $R\bar{3}m$ space group. Rietveld refinement was conducted to determine the detailed structure, and the refinement results are shown in Table S1. Figures 1(b) and 1(c) show the microscale particle morphology of NCM811, which exhibits a spherical geometry composed of primary particles. The surface of pristine NCM811 is dense and smooth, while the secondary particles exhibit a typical diameter of ∼ 7.86 μm (Fig. S1). To directly probe the lattice geometry, Fig. 1(d) shows the TEM image of NCM811 along the (003) plane, where a well-ordered layered structure can be directly observed. The (003) plane exhibits a lattice spacing of 0.465 nm, which is consistent with the XRD results. The structural and microscale morphological characterizations indicate that the pristine NCM811 exhibits a prevailing well-ordered layered structure. To characterize the electrochemical performance, the NCM811 cathode was cycled in a coin cell. Figure 1(e) shows the typical charge-discharge curves of NCM811 at 1C in the voltage range 3.0–4.5 V. NCM811 exhibits a first discharge capacity of 186.2 mAh/g and a capacity retention rate of 69.4% after 100 cycles (Fig. S2). Figure 1(b) further shows the corresponding dQ/dV curves within 100 cycles. Several phase transition peaks can be detected and well labeled in the dQ/dV curve. The dQ/dV peaks at 3.76 V, 4.03 V, and 4.23 V can be attributed to the H1–M, M–H2, and H2–H3 phase transitions, respectively.[18] During prolonged cycling, the H1–M peak first intensifies and then gradually declines, whereas the M–H2 peak decreases monotonically and ultimately vanishes. Owing to increasing impedance, both peaks continuously shift toward higher voltages. More importantly, sustained electrochemical cycling leads to a continuous weakening of the H2–H3 transition peak. The reversibility of this transition is intimately correlated with the degradation of the electrochemical performance.[19] The accumulation of these irreversible phase transitions in NCM811 over long-term cycling eventually leads to the deterioration of electrochemical performance. These electrochemical results are consistent with literature reports and demonstrate typical NCM811 properties,[19,20] which provides a solid foundation for subsequent investigations into thermal decay.

To characterize thermally induced microstructural changes, SEM was utilized to probe the microscale morphological evolution of delithiated NCM811. Figures 2(a)–2(d) correspond to $Li_{0.3}$NCM-25 °C, $Li_{0.3}$NCM-150 °C, $Li_{0.3}$NCM-300 °C, and $Li_{0.3}$NCM-450 °C, respectively. Compared with pristine NCM811 in Fig. 1(c), $Li_{0.3}$NCM-25 °C exhibits a porous surface, which can be attributed to electrochemical erosion caused by deposited surface species.

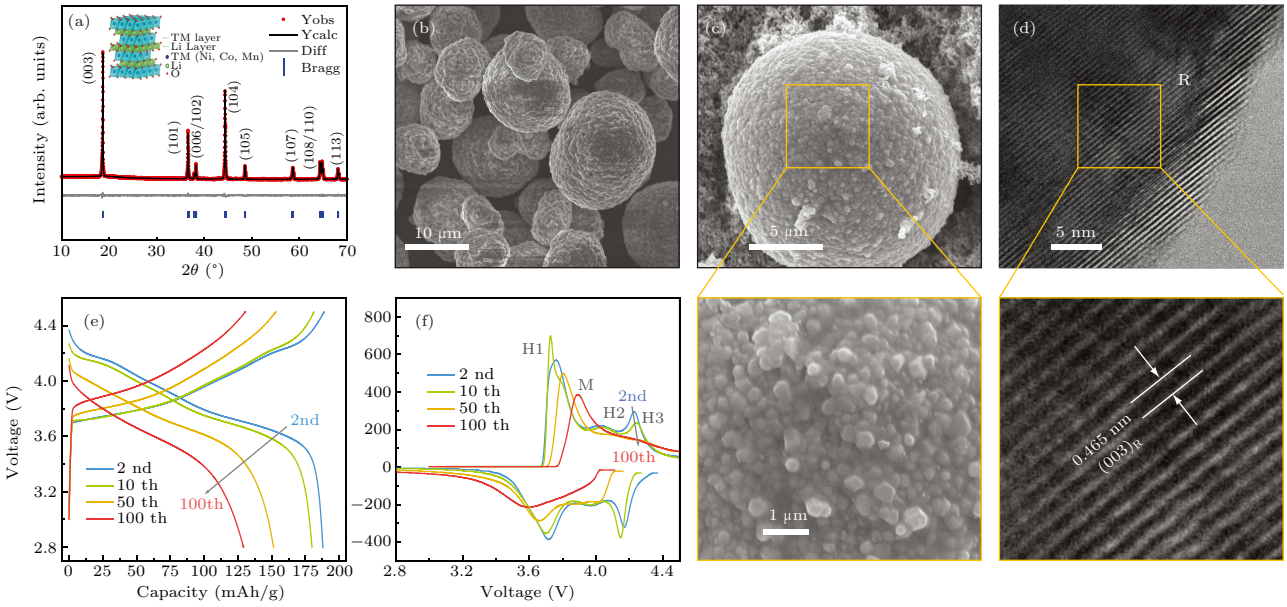


Fig. 1. (a) XRD pattern of NCM811, with lattice structure and reference data (ICDD No. 01-070-4314) indicated. Low-magnification (b) and high-magnification (c) SEM images of NCM811. (d) TEM image of NCM811 particles showing the lattice distance along the *c*-axis. (e) Typical charge-discharge profiles and corresponding dQ/dV curves of NCM811 over 100 cycles.

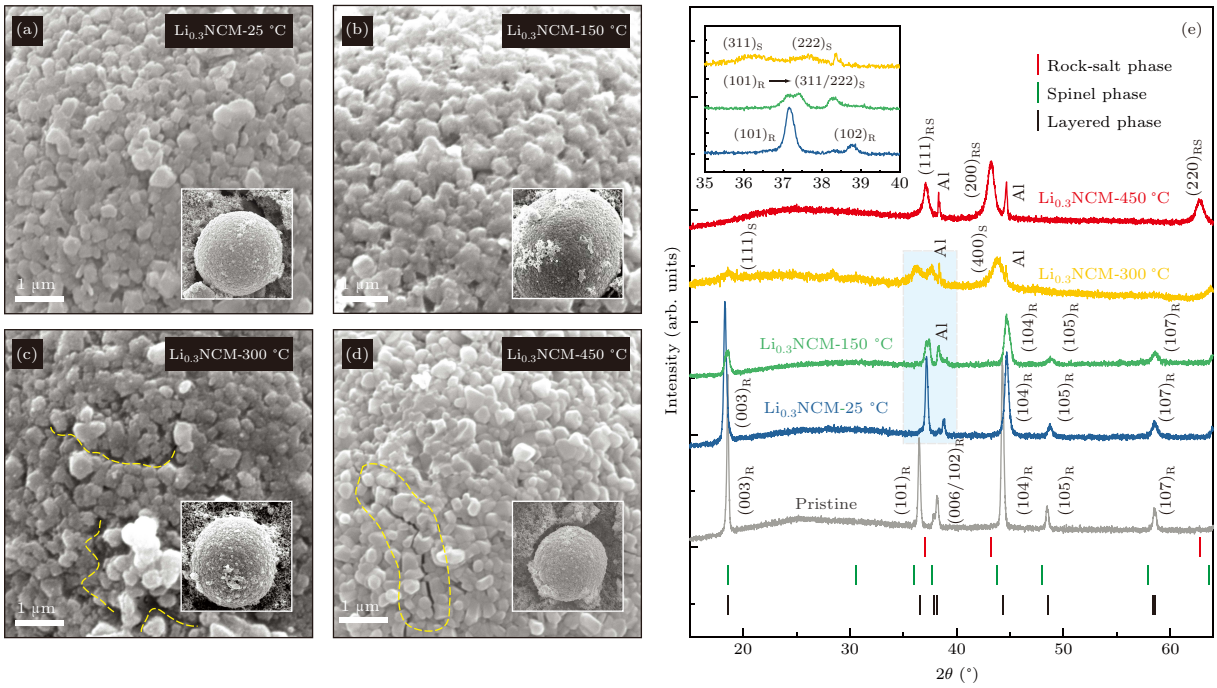


Fig. 2. SEM images of delithiated NCM811 at increasing temperatures: (a) $Li_{0.3}$NCM-25 °C, (b) $Li_{0.3}$NCM-150 °C, (c) $Li_{0.3}$NCM-300 °C, and (d) $Li_{0.3}$NCM-450 °C. (e) Corresponding XRD patterns at different states. Reference patterns for layered NCM811 (ICDD No. 01-070-4314), spinel $LiMn_2O_4$ (ICDD No. 01-070-3120), and rock-salt NiO (ICDD No. 00-001-1239) are included. The inset shows an enlarged view from 35° to 40°.

When the sample is heated to 150 °C, the primary particles on the surface become even more isolated from each other. When the temperature is increased to 300 °C, signs of cracking begin to emerge. Finally, when the temperature reaches 450 °C, obvious cracks appear on the particle surface, as indicated by the yellow dashed box in Fig. 2(d). The surface morphology evolves from a dense structure to a porous one, and ultimately to crack formation, which can be attributed to accumulated internal stress. Thermally induced phase transformation and lattice mismatch are likely the intrinsic origins. To verify such structural changes, the XRD evolution with temperature is shown in Fig. 2(e). Compared with pristine NCM811, $Li_{0.3}$NCM-25 °C shows that the $(003)_R$ peak shifts to a lower angle at 18.27°, indicating an increased layer spacing after delithiation. This observation is consistent with the work of Sun *et al.*[21] It should be noted that different studies report either an increase or a decrease in the *c*-axis lattice parameter at Li_{1-x} with $x \approx 0.7$,[20,22] and these discrepancies can be attributed to variations in electrode materials and testing conditions. For $Li_{0.3}$NCM-150 °C, the intensities of the $(003)_R$, $(105)_R$, and $(107)_R$ peaks of the layered phase are significantly reduced, indicating that the layered phase begins to fade gradually. Meanwhile, the $(101)_R$ peak begins to split near 37°, transforming into the $(311)_S$ and $(222)_S$ peaks of the spinel phase within the *Fd3m* space group (enlarged view in the inset).[6] The XRD evolution indicates that layered NCM starts to transform into the spinel phase as low as 150 °C. In $Li_{0.3}$NCM-300 °C, peaks from the layered phase, including $(105)_R$ and $(107)_R$, completely disappear, while spinel-phase-related $(311)_S$, $(222)_S$, and $(400)_S$ peaks at 36.39°, 37.65°, and 43.78° remain. The diffraction peak evolution indicates that the layered structure has entirely transformed into the spinel phase at 300 °C. When the temperature is further increased to 450 °C, the spinel phase peaks completely disappear, and diffraction peaks corresponding to the rock-salt $(111)_{RS}$, $(200)_{RS}$, and $(220)_{RS}$ emerge at 37.08°, 43.15°, and 62.68°, respectively. The XRD peak evolution is consistent with previous works by Yang *et al.*[6] and Nam *et al.*[5]. Such changes imply that the delithiated NCM811 fully transforms from the spinel to the rock-salt phase at 450 °C. The structural transformation from the layered ($R\bar{3}m$) to spinel ($Fd3m$), and finally to rock-salt ($Fm3m$) phase is consistent with the SEM morphology change, where internal strain from lattice mismatch gradually leads to crack formation.

To directly probe the local structural changes during thermal decay, Figs. 3(a)–3(d) present TEM images of $Li_{0.3}$NCM at 25 °C, 150 °C, 300 °C, and 450 °C, respectively. As shown in Fig. 3(a), $Li_{0.3}$NCM-25 °C exhibits a well-ordered layered structure. The (003) plane is clearly resolved with a lattice spacing of 0.473 nm, which is larger than the pristine value of 0.465 nm in Fig. 1(d). This expansion arises from enhanced TMO_2 slab repulsion due to reduced Li screening and is consistent with the XRD peak shift.

At 150 °C, $Li_{0.3}$NCM largely retains its layered structure, as shown in Fig. 3(b) and further confirmed by the fast fourier transform (FFT) image of region i. However, significant transition-metal (TM) migration from the TM layer into the Li layer is detected, especially near the particle surface

(region ii). The FFT of this region confirms that the layered framework remains intact, indicating that while the bulk structure is preserved, TM migration initiates the gradual transformation from layered to spinel.

When the temperature rises to 300 °C (Fig. 3(c)), the bulk of $Li_{0.3}$NCM has predominantly transformed into the spinel phase, as evidenced by the 0.244 nm lattice spacing of the (222) plane observed in region iii (additional details in Fig. S3). On the particle surface, partial rock-salt domains are detected and validated by the FFT pattern of region iv. Finally, Fig. 3(d) shows that $Li_{0.3}$NCM-450 °C is fully converted into the rock-salt phase.

The TEM results thus capture the local structural evolution of NCM811 during thermal treatment, revealing that the material undergoes a stepwise phase transition — from layered, to spinel, and ultimately to rock-salt — with increasing temperature. Notably, phase transformation at the particle surface tends to precede that of the bulk.

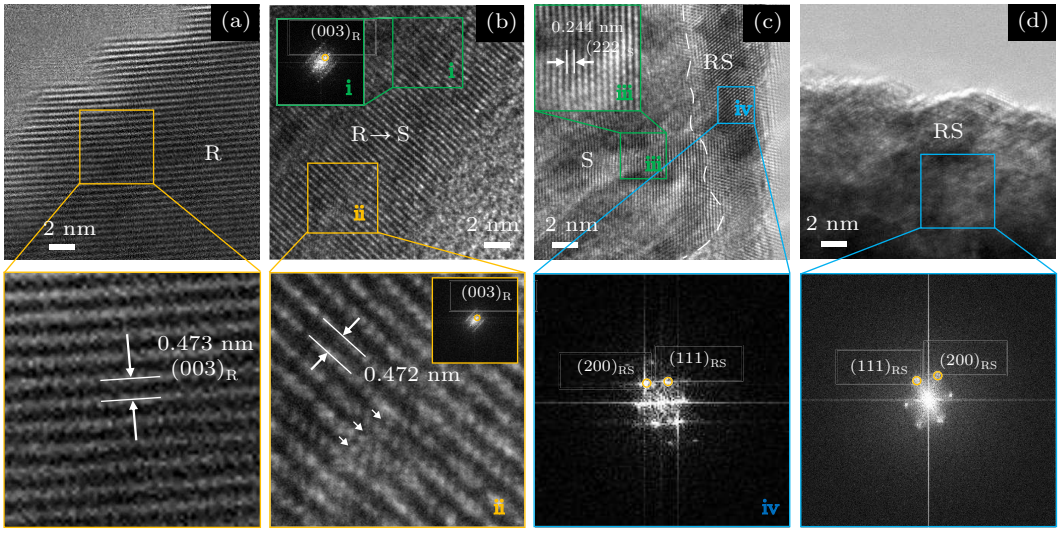


Fig. 3. TEM images of delithiated NCM811 at increasing temperatures: (a) $Li_{0.3}$NCM-25 °C, (b) $Li_{0.3}$NCM-150 °C, (c) $Li_{0.3}$NCM-300 °C, and (d) $Li_{0.3}$NCM-450 °C.

To clarify the fundamental roles of individual elements during the thermal failure process, sXAS is employed to probe the electronic state evolution of NCM811 with increasing temperature. By virtue of TEY and PFY detection modes, sXAS can simultaneously provide information from both the surface and the bulk. The TEY spectra of the Ni L_3-edge in Fig. 4(a), located in the range 850–857 eV, correspond to $2p_{3/2}$ to 3d orbital transitions. For pristine NCM811, the peak features closely resemble those of NiO, indicating the predominance of Ni^{2+} on the surface.[23] In contrast, the PFY spectra of the Ni L_3-edge of pristine NCM811 in Fig. 4(b) exhibit features more similar to Ni^{3+}, suggesting that Ni^{3+} dominates in the bulk, substantially differing from the surface composition.

Additionally, the pre-edge features of the O K-edge can be employed to probe the chemical states of transition metals (TM), as they arise from hybridization between TM 3d and O 2p states.[24] Given the high proportion of Ni in NCM811, the pre-edge features of the O K-edge primarily reflect the hybridization characteristics of Ni. The PFY spectra of the O K-edge in Fig. 4(d) exhibit a distinct peak at ∼ 528 eV, labeled as A, confirming the presence of bulk Ni^{3+} in the pristine sample. In contrast, the TEY spectra reveal a Ni^{2+} feature at ∼ 532 eV, consistent with the surface-sensitive TEY data of the Ni L_3-edge. A dominant feature at ∼ 533 eV, labeled as peak C in the TEY spectra of the O K-edge (Fig. 4(c)), is typically attributed to C=O bonds, indicating a substantial amount of Li_2CO_3 on the surface.[25] This is further supported by a weaker feature, labeled as C′, in the 532–533 eV range of the PFY spectra (Fig. 4(d)), which arises from overlapping contributions of C=O bonds and Ni^{2+}. The surface coating is reported to originate from highly reactive residual lithium.[26] Similar to the analysis of the Ni L-edge, the peak at ∼ 779 eV in Figs. 4(e) and 4(f) indicates that Co^{3+} is the dominant oxidation state on both the surface and in the bulk.

Upon delithiation to 4.5 V ($Li_{0.3}$NCM-25 °C), a peak at ∼ 855 eV emerges sharply in both the TEY and PFY spectra of the Ni L_3-edge. This spectral evolution is typically attributed to TM oxidation for charge compensation. However, this feature has also been reported to result from the formation of O-hole states with the $|3d^8L^2\rangle$ electronic configuration, originating from a ligand-to-metal charge transfer (LMCT) process.[27] This assignment is further supported by the evolution of the O K-edge features. Specifically, the shift of pre-edge feature A (marked as A′), together with its increased intensity in both TEY and PFY spectra, indicates the formation of O-hole states in both the surface and the bulk during delithiation.[27] This unique form of oxygen activation alters Ni–O hybridization, as evidenced by the distinct feature in the resonant O $K\alpha$ XES spectrum (Fig. S5), consistent with previous reports.[27–29]

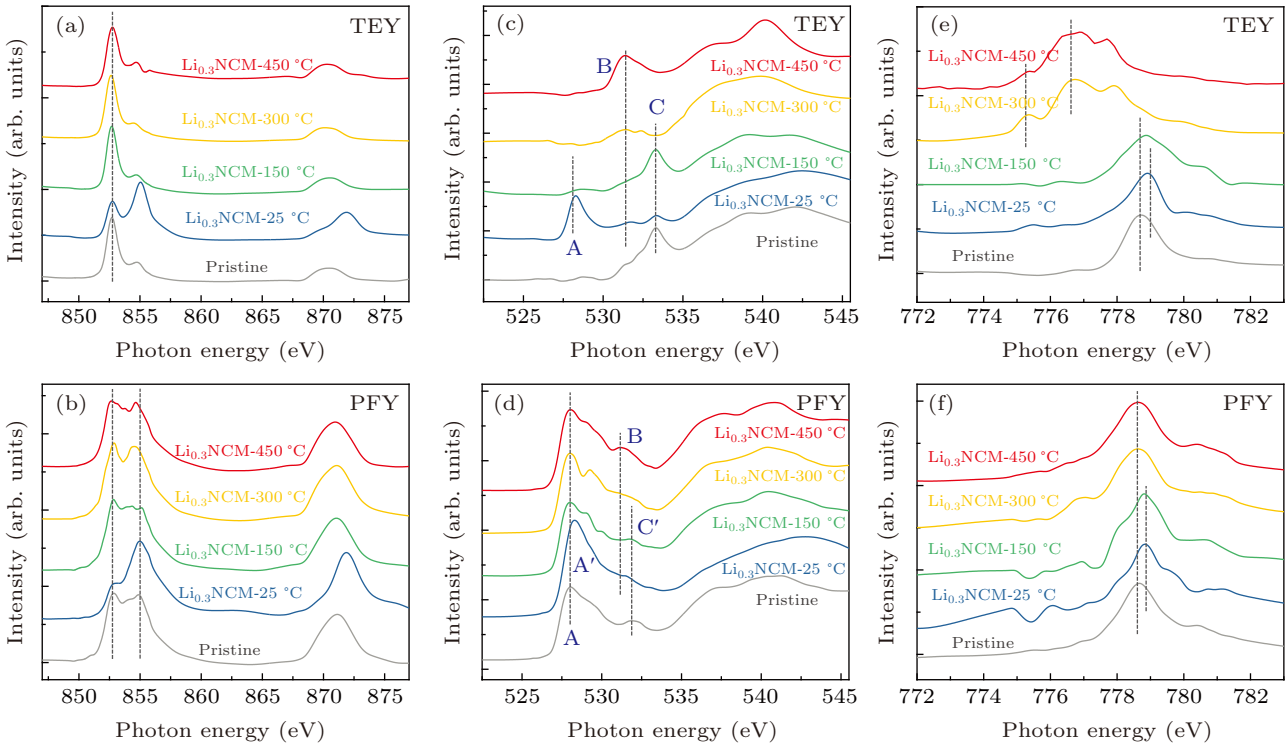


Fig. 4. The sXAS spectra of NCM811 at different states: Ni *L*-edge in (a) TEY and (b) PFY mode, O *K*-edge in (c) TEY and (d) PFY mode, and Co *L*-edge in (e) TEY and (f) PFY mode.

Furthermore, the significant decrease of features C and C′ indicates the decomposition of Li_2CO_3 at 4.5 V, consistent with previous electrochemical studies.[25,30,31] In addition, a small feature at ∼ 532 eV, labeled as B, appears in both TEY and PFY spectra, typically assigned to electrochemically inactive Ni^{2+} species such as rock-salt NiO. However, the substantial decrease of feature B, along with the concurrent increase of feature A′ in the TEY spectra, provides evidence for the electrochemical activity of Ni^{2+} at the surface. This observation aligns with previous reports of a surface rock-salt-like $Li_xNi_{1-x}O$ phase that retains Li-ion activity, likely formed by Ni–Li intermixing.[32] While Mn^{4+} in NCM811 remains electrochemically inert, as shown in Fig. S4, Co^{3+} is oxidized to Co^{4+} upon delithiation, as indicated by the blue-shift of the Co L_3-edge in Fig. 4(f). This behavior closely resembles that observed in the $LiCoO_2$ cathode.[33]

When $Li_{0.3}$NCM is heated to 150 °C, bulk Ni reverts to a state similar to pristine NCM811, as revealed by the PFY spectra. This change suggests the disappearance of O-hole states in the $|3d^8L^2\rangle$ electronic configuration due to the release of O_2. The formation of O–O bonds becomes energetically favorable during heating, as the lattice parameter along the *c*-axis decreases significantly because of the H2–H3 transition, as shown in Fig. 2(e).[34–36] In contrast, surface Ni is reduced to Ni^{2+}, as revealed by the TEY spectra. The electron transfer toward surface Ni sites suggests that O-hole states in both the $|3d^8L\rangle$ and $|3d^8L^2\rangle$ configurations dimerize to form O_2 and are subsequently released — a process analogous to the redox-coupling mechanism in lithium-rich cathodes.[37,38] Although surface oxygen is generally more reactive than bulk oxygen, this observation implies that O_2 release from both the surface and the bulk occurs almost simultaneously — or at least within a very short time frame — considering that $Li_{0.3}$NCM was heat treated for only 10 minutes. This result is consistent with findings from the Wang group, where both the surface layer and the bulk exhibit high oxygen vacancy concentrations as the Ni ratio increases to 0.8.[10] Moreover, thermogravimetric analysis (TGA) in Fig. S6 indicates that the transformation to the spinel phase starts from ∼ 200 °C, suggesting that O_2 release precedes the structural phase transition. Therefore, destabilization of O-hole states is likely the initiating cause of thermal failure in Ni-rich layered cathodes. Despite the short treatment duration, a weak spinel signal is observed in the XRD patterns in Fig. 2(e). This may be attributed to surface-dominant Ni^{2+}, which tends to migrate to tetrahedral sites, facilitating local spinel formation. Indeed, small spinel domains near the surface are confirmed by the corresponding TEM image in Fig. 3(b). In contrast, Ni^{3+} ions in the bulk are less likely to migrate through tetrahedral sites. Simultaneously, O_2 release increases the Coulombic repulsion between adjacent Ni^{3+} ions, destabilizing the crystal lattice. This structural degradation is consistent with the pronounced decrease in XRD intensity from $Li_{0.3}$NCM-25 °C to $Li_{0.3}$NCM-150 °C in Fig. 2(e). In addition to the formation of Ni^{2+}, a significant amount of Li_2CO_3 is found to re-form on the surface, as indicated by the O *K*-edge spectra in Fig. 4(c). This likely results from the reaction between residual components of the cathode–electrolyte interphase (CEI) layer and the

released O_2.[39,40] Moreover, the electrons left behind during O_2 evolution also contribute to the reduction of Co, as shown in Fig. 4(e). Unlike Ni, all Co^{4+} ions on the surface are reduced to Co^{3+}, indicating that Co is relatively more stable.

Upon further heating $Li_{0.3}$NCM to 300 °C, an increased accumulation of surface Ni^{2+} is observed, accompanied by additional O_2 release and complete decomposition of the reformed Li_2CO_3, as shown by the TEY data of the O *K*-edge. These changes lead to a notable increase in the XRD signal corresponding to the spinel phase and even the emergence of the RS phase, as confirmed by the TEM images. Additionally, a small amount of Ni^{2+} may form in the bulk, as indicated by the significant evolution in the PFY spectra of the Ni L_3-edge. This observation aligns with the enhanced spinel signal observed in the XRD patterns and the widespread distribution of spinel zones away from the surface in the TEM images. Another notable transformation is the reduction of Co^{3+} to Co^{2+} on the surface, which can also be attributed to severe oxygen loss. In contrast, Co ions in the bulk remain in the 3+ oxidation state throughout the heat treatment, further confirming their superior thermal stability. Comparing $Li_{0.3}$NCM-300 °C and $Li_{0.3}$NCM-450 °C, most spectral features exhibit minimal change. However, the O *K*-edge spectra show a relatively pronounced evolution of feature B, indicating a further increase of bulk Ni^{2+} — undoubtedly a result of O_2 release. The extensive oxygen depletion, along with the high concentrations of Ni^{3+} and Co^{3+}, leads to progressive destabilization of the crystalline framework. This structural degradation is consistent with the amorphization observed in the TEM image in Fig. 3(d). Finally, it is worth noting that Mn^{4+}, as shown in Fig. S4, remains largely unchanged throughout the entire heating process, highlighting its excellent thermal stability.

According to the above discussion, the initial oxidation state of bulk Ni in NCM811 is predominantly Ni^{3+}. Upon removal of 0.7 mol of Li, a large number of oxygen-hole states in the $|3d^8L^2\rangle$ configuration are formed. These O-hole states become unstable upon heating to 150 °C, leading to oxygen dimerization and subsequent O_2 release. Given that the bulk phase transition starts from ∼ 200 °C, we propose that the instability of the $|3d^8L^2\rangle$ oxygen-hole state is the fundamental driving force for thermal failure. The loss of lattice oxygen increases the Coulombic repulsion between adjacent Ni^{3+} ions, ultimately causing structural amorphization in the bulk. In contrast, the initial state of surface Ni is Ni^{2+}, likely existing in a RS phase $Li_xNi_{1-x}O$. As 0.7 mol of Li is removed, oxygen-hole states similar to those in the bulk are also generated on the surface. However, at 150 °C, not only the $|3d^8L^2\rangle$ but also the $|3d^8L\rangle$ configurations become unstable. The resulting loss of surface oxygen reduces Ni^{3+} to Ni^{2+}, thereby facilitating the formation of a spinel phase on the surface as early as 150 °C. Although surface oxygen is intrinsically less stable than bulk oxygen, the presence of oxygen-hole states in $|3d^8L^2\rangle$ may cause oxygen loss from both regions to occur almost simultaneously. As the temperature increases to 300 °C, bulk oxygen loss intensifies, accompanied by the formation of a small amount of Ni^{2+}, which further promotes the development of a bulk spinel phase. At 450 °C, a significant increase in bulk Ni^{2+} is observed, corresponding to the emergence of a bulk RS phase. Compared with Ni, Co exhibits superior thermal stability: surface Co is fully reduced to Co^{2+} at 300 °C, whereas bulk Co remains in the Co^{3+} state throughout the entire heating process. Meanwhile, Mn^{4+} is the most stable element, showing no obvious change (Fig. S4), and thus functions as a structural pillar during the thermal decay process.

Based on the preceding discussion, a schematic illustration of the thermal degradation of NCM811 is shown in Fig. S7. The critical electronic state, namely the O-hole state, triggers oxygen-vacancy formation accompanied by O_2 release, which in turn drives structural transitions and ultimately results in thermal instability. From these mechanistic insights, rational strategies can be proposed to enhance the thermal stability of Ni-rich cathodes. Optimization should focus on suppressing the formation of $|3d^8L\rangle$ and $|3d^8L^2\rangle$ states. Introducing high-valence cations (e.g., W^{6+}, Nb^{5+}) or high-covalency anions (e.g., F^-) represents a promising approach. Cation substitution may reduce the probability of forming $|3d^8L\rangle$ and $|3d^8L^2\rangle$ states, while stronger M–O bonds and more delocalized oxygen-hole states can raise the thermal trigger threshold. Partial substitution of O^{2-} with F^- forms strong ionic bonds with cations, which may further enhance lattice stability. Since surface Ni undergoes more complete reduction and thus triggers structural transitions at an earlier stage, surface protection (e.g., Li_3PO_4 or Al_2O_3 coatings) provides a practical means to suppress these processes and improve thermal stability. Overall, identifying oxygen as the trigger for Ni-rich cathode thermal decay opens a clear avenue toward designing Ni-rich cathodes with high energy density and improved thermal safety, thereby paving the way for large-scale applications.

4. Conclusion

In this work, we analyzed the structural changes and elemental roles in delithiated NCM811 during thermal decay from both surface and bulk perspectives. XRD and TEM results indicate that delithiated NCM811 undergoes a phase transformation from the layered to spinel and finally to rock-salt phase during thermal runaway, with surface phase changes preceding those in the bulk. The mechanism of thermal failure, which involves these phase transitions, was then systematically studied by element-sensitive sXAS in TEY and PFY modes. The bulk of NCM811 is primarily composed of Ni^{3+}. The oxygen hole states formed upon delithiation are thermally unstable and release O_2 upon heating, which serves as the un-

derlying cause of thermal failure in the NCM811 cathode. Although surface oxygen is inherently less stable, the presence of similar oxygen hole states leads to surface and bulk degradation occurring almost simultaneously. Therefore, the evolution of oxygen hole states is identified as the actual origin and fundamental driving force for subsequent structural distortion and lattice collapse during thermal decay. Consequently, stabilizing oxygen hole states is the key to further improving the high-temperature electrochemical performance and safety of Ni-rich cathodes. This study deepens the understanding of the failure mechanism in NCM811 and highlights the tuning of oxygen hole states as a fundamental strategy to enhance its thermal stability, which is significant for the further development of Ni-rich cathodes.

Acknowledgments

This project was supported by the Science and Technology Commission of Shanghai Municipality (Grant No. 22560780300), the National Natural Science Foundation of China (Grant Nos. 22309097 and 52130202), the Shandong Provincial Natural Science Foundation (Grant Nos. 2023KJ228 and ZR2021QE061), the Youth Innovation Technology Project of Higher Education Institutions in Shandong Province (Grant No. 2022KJ139), and the Shanghai Soft X-ray Free-Electron Laser Facility beamline project. The authors thank beamline 20U (31124.02.SSRF.BL20U2) of SSRF and UXS of sXFEL for the XES measurements, and beamline BL02B (31124.02.SSRF.BL02B02) of SSRF for the sXAS measurements.

References

[1] Liu W, Oh P, Liu X, Lee M J, Cho W, Chae S, Kim Y and Cho J 2015 *Angew. Chem. Int. Ed.* **54** 4440
[2] Myung S T, Maglia F, Park K J, Yoon C S, Lamp P, Kim S J and Sun Y K 2017 *ACS Energy Lett.* **2** 196
[3] Zhang S S 2020 *Energy Storage Mater.* **24** 247
[4] Hwang S, Kim S M, Bak S M, Kim S Y, Cho B W, Chung K Y, Lee J Y, Stach E A and Chang W 2015 *Chem. Mater.* **27** 3927
[5] Bak S M, Hu E, Zhou Y, Yu X, Senanayake S D, Cho S J, Kim K B, Chung K Y, Yang X Q and Nam K W 2014 *ACS Appl. Mater. Inter.* **6** 22594
[6] Nam K W, Bak S M, Hu E, Yu X, Zhou Y, Wang X, Wu L, Zhu Y, Chung K Y and Yang X Q 2013 *Adv. Funct. Mater.* **23** 1047
[7] Hwang S, Chang W, Kim S M, Su D, Kim D H, Lee J Y, Chung K Y and Stach E A 2014 *Chem. Mater.* **26** 1084
[8] Liu X, Xu G L, Yin L, Hwang I, Li Y, Lu L, Xu W, Zhang X, Chen Y, Ren Y, Sun C J, Chen Z, Ouyang M and Amine K 2020 *J. Am. Chem. Soc.* **142** 19745
[9] Lee S, Jin W, Kim S H, Joo S H, Nam G, Oh P, Kim Y K, Kwak S K and Cho J 2019 *Angew. Chem. Int. Ed.* **58** 10478
[10] Wei Z, Liang C, Jiang L, Wang L, Cheng S, Peng Q, Feng L, Zhang W, Sun J and Wang Q 2022 *Energy Storage Mater.* **47** 51
[11] Li J, Hua H, Kong X, Yang H, Dai P, Zeng J and Zhao J 2022 *Energy Storage Mater.* **46** 90
[12] Yoon W S, Haas O, Muhammad S, Kim H, Lee W, Kim D, Fischer D A, Jaye C, Yang X Q and Balasubramanian M 2014 *Sci. Rep.* **4** 6827
[13] Li Q, Yan S and Yang W 2020 *J. Chem. Phys.* **152** 140901
[14] Chen S, Jiao S, Liang Q, Li P, Yin J, Li Q, Yu X and Li Q 2024 *Anal. Chem.* **96** 8021
[15] Xie J, Chen J, Guo L, Li Y, Wang Y, Zheng S, Zhang N, Meng J, Zhang K, Li Q, Weng T C, Yu P and Liu X 2025 *ACS Nano* **19** 3931
[16] Li P, Li Y, Liang Q, Niu Y, Zheng S, Zhuo Z, Luo Y, Liang B, Yang D, Yin J, Chen S, Ye W, Pan Y, Li Q, Yu P, Liu X and Li Q 2025 *Carbon Energy* **7** e699
[17] Li Y, Zheng S, Xie J, Shen L, Li J, Meng J, Zhang N, Li Q, Weng T C, Liu X and Yu P 2024 *ACS Energy Lett.* **9** 4864
[18] Gomez-Martin A, Reissig F, Frankenstein L, Heidbuchel M, Winter M, Placke T and Schmuch R 2022 *Adv. Energy Mater.* **12** 2103045
[19] Wu F, Liu N, Chen L, Su Y, Tan G, Bao L, Zhang Q, Lu Y, Wang J, Chen S and Tan J 2019 *Nano Energy* **59** 50
[20] Wang L, Liu T, Wu T and Lu J 2022 *Nature* **611** 61
[21] Sun Y, Wang C, Huang W, Zhao G, Duan L, Liu Q, Wang S, Fraser A, Guo H and Sun X 2023 *Angew. Chem. Int. Ed.* **62** e202300962
[22] Li W, Asl H Y, Xie Q and Manthiram A 2019 *J. Am. Chem. Soc.* **141** 5097
[23] Qinghao L, Ruimin Q, Wray L A, Jun C, Zengqing Z, Yanxue C, Shishen Y, Feng P, Zahid H and Wanli Y 2016 *J. Phys. D: Appl. Phys.* **49** 413003
[24] Roychoudhury S, Qiao R, Zhuo Z, Li Q, Lyu Y, Kim J H, Liu J, Lee E, Polzin B J, Guo J, Yan S, Hu Y, Li H, Prendergast D and Yang W 2021 *Energy Environ. Mater.* **4** 246
[25] Zhuo Z, Dai K, Qiao R, Wang R, Wu J, Liu Y, Peng J, Chen L, Chuang Y D, Pan F, Shen Z X, Liu G, Li H, Devereaux T P and Yang W 2021 *Joule* **5** 975
[26] Cho D H, Jo C H, Cho W, Kim Y J, Yashiro H, Sun Y K and Myung S T 2014 *J. Electrochem. Soc.* **161** A920
[27] Ogley M J W, Menon A S, Pandey G C, Páez Fajardo G J, Johnston B J, McClelland I, Majherova V, Huband S, Tripathy D, Temprano I, Agrestini S, Celorrio V, Pérez G E, Booth S G, Grey C P, Cussen S A and Piper L F J 2024 *Joule* **9** 101775
[28] Lee G H, Lee S, Zhang J, Rinkel B L D, Crafton M J, Zhuo Z, Choi Y, Li J, Yang J, Heo J W, Park B, McCloskey B D, Avdeev M, Yang W and Kang Y M 2024 *Energy Environ. Sci.* **17** 9154
[29] Juelsholt M, Chen J, Pérez-Osorio M A, Rees G J, De Sousa Coutinho S, Maynard-Casely H E, Liu J, Everett M, Agrestini S, Garcia-Fernandez M, Zhou K J, House R A and Bruce P G 2024 *Energy Environ. Sci.* **17** 2530
[30] Lebens-Higgins Z W, Sallis S, Faenza N V, Badway F, Pereira N, Halat D M, Wahila M, Schlueter C, Lee T L, Yang W, Grey C P, Amatucci G G and Piper L F J 2018 *Chem. Mater.* **30** 958
[31] Piao J Y, Liu X C, Wu J, Yang W, Wei Z, Ma J, Duan S Y, Lin X J, Xu Y S, Cao A M and Wan L J 2018 *ACS Appl. Mater. Inter.* **10** 22896
[32] Shah N A, Páez Fajardo G J, Banerjee H, Pandey G C, Menon A S, Ans M, Majherova V, Bree G, Bolloju S, Grinter D C, Ferrer P, Thakur P K, Lee T L, Loveridge M J, Morris A J, Grey C P and Piper L F J 2025 *ACS Energy Lett.* **10** 1313
[33] Long X H, Wu Y R, Zhang N, Yu P F, Feng X F, Zheng S, Fu J M, Liu X S, Liu N, Wang M, Xu L M, Chen J M and Lee J M 2018 *Chin. Phys. B* **27** 107802
[34] Noh H J, Youn S, Yoon C S and Sun Y K 2013 *J. Power Sources* **233** 121
[35] Li W, Reimers J N and Dahn J R 1993 *Solid State Ionics* **67** 123
[36] Hu E, Li Q, Wang X, Meng F, Liu J, Zhang J N, Page K, Xu W, Gu L, Xiao R, Li H, Huang X, Chen L, Yang W, Yu X and Yang X Q 2021 *Joule* **5** 720
[37] Saubanere M, McCalla E, Tarascon J M and Doublet M L 2016 *Energy Environ. Sci.* **9** 984
[38] Sathiya M, Rousse G, Ramesha K, Laisa C P, Vezin H, Sougrati M T, Doublet M L, Foix D, Gonbeau D, Walker W, Prakash A S, Ben Hassine M, Dupont L and Tarascon J M 2013 *Nat. Mater.* **12** 827
[39] Li Q, Liang Q, Zhang H, Jiao S, Zhuo Z, Wang J, Li Q, Zhang J N and Yu X 2023 *Angew. Chem. Int. Ed.* **62** e202215131
[40] Li Q, Wang Y, Wang X, Sun X, Zhang J N, Yu X and Li H 2020 *ACS Appl. Mater. Inter.* **12** 2319